Phase transition and electronic structure evolution of MoTe_{2} induced by W substitution

Wencan Jin, Theanne Schiros, Yi Lin, Junzhang Ma, Rui Lou, Zhongwei Dai, Jie-Xiang Yu, Daniel Rhodes, Jerzy T. Sadowski, Xiao Tong, Tian Qian, Makoto Hashimoto, Donghui Lu, Jerry I. Dadap, Shancai Wang, Elton J. G. Santos, Jiadong Zang, Karsten Pohl, Hong Ding, James Hone, Luis Balicas, Abhay N. Pasupathy, and Richard M. Osgood, Jr.

Phys. Rev. B **98**, 144114 — Published 31 October 2018
DOI: 10.1103/PhysRevB.98.144114

Phase transition and electronic structure evolution of $MoTe_2$ induced by W substitution

Wencan Jin,[1,*] Theanne Schiros,[2] Yi Lin,[1] Junzhang Ma,[3] Rui Lou,[4] Zhongwei Dai,[5] Jie-Xiang Yu,[5] Daniel Rhodes,[6] Jerzy T. Sadowski,[7] Xiao Tong,[7] Tian Qian,[3] Makoto Hashimoto,[8] Donghui Lu,[8] Jerry I. Dadap,[1] Shancai Wang,[4] Elton J. G. Santos,[9] Jiadong Zang,[5] Karsten Pohl,[5] Hong Ding,[3] James Hone,[1] Luis Balicas,[6] Abhay N. Pasupathy,[1,†] and Richard M. Osgood, Jr[1,‡]

[1]*Columbia University, New York, New York 10027, USA*
[2]*Fashion Institute of Technology, New York, New York 10001, USA*
[3]*Beijing National Laboratory for Condensed Matter Physics,*
and Institute of Physics, Chinese Academy of Sciences, Beijing 100190, China
[4]*Department of Physics, Renmin University of China, Beijing 100872, China*
[5]*University of New Hampshire, Durham, New Hampshire 03824, USA*
[6]*Florida State University, Tallahassee, Florida 32306, USA*
[7]*Center for Functional Nanomaterials, Brookhaven National Laboratory, Upton, New York 11973, USA*
[8]*Stanford Synchrotron Radiation Light Source, SLAC National Accelerator Laboratory, Menlo Park, California, 94025, USA*
[9]*School of Mathematics and Physics, Queen's University Belfast, BT71NN, UK*

The transition metal dichalcogenide compounds $MoTe_2$ and WTe_2 are polymorphic with both semiconducting and metallic phases. The thermodynamically stable phase of WTe_2 at room temperature is orthorhombic and metallic, and displays a wide range of interesting phenomena including type-II Weyl fermions, titanic magnetoresistance and superconductivity in bulk, and quantum spin Hall insulator behavior in the monolayer case. On the other hand, the stable phase of $MoTe_2$ at room temperature is a trigonal prismatic semiconductor that has a direct gap in the monolayer with strong spin-orbit coupling. The alloy series $Mo_{1-x}W_xTe_2$ thus offers the possibility of tuning the structural and, consequently, electronic phases via tuning of the composition. Here, we report comprehensive studies of the electronic structure of $Mo_{1-x}W_xTe_2$ alloys using angle-resolved photoemission spectroscopy and first-principle calculations as a function of composition. At room temperature, we find a sharp boundary between the orthorhombic and trigonal prismatic phases at $x = 0.10$ using structural characterization. We also show that by compositional tuning it is possible to control the band inversion in this series of compounds, thus yielding important consequences for topological surface states.

I. INTRODUCTION

Transition metal dichalcogenides (TMDCs, MX_2, M=Mo, W; X=Se, Te) are polymorphic with different crystal structures, including trigonal prismatic $2H$ phase (Fig. 1(a)), monoclinic $1T$' phase, and orthorhombic T_d phase (Fig. 1(d)). These phases provide an important platform for exploring exotic physics and novel device applications. The semiconducting $2H$-phase TMDCs in monolayer form consists of a layer of hexagonally arranged transition metal atoms sandwiched between two layers of chalcogen atoms. In monolayer $2H$-TMDCs, the sizeable direct band gap [1–3] and valley degree of freedom [4–6] make this phase remarkably appealing for electronics [7], and spin- and valley-tronics devices [8, 9]. Recently, the metallic $1T$' and T_d phase have attracted interest due to the presence of band inversion in these phases, making them important candidates for realizing novel topological quantum phenomena. The semimetallic $1T$' phase exhibits a distorted octahedral structure with an inclined stacking angle of ∼93.9°, which retains a centrosymmetric $P2_1/m$ space group. In contrast, in the orthorhombic T_d phase, the stacking angle is exactly 90°, which breaks inversion symmetry (space group $Pmn2_1$) [10]. The T_d phase displays a number of unique electronic properties in both the bulk and monolayer forms. Bulk crystals of both T_d-WTe_2 [11, 12] and T_d-$MoTe_2$ [13] display a large, non-saturating magnetoresistance, possibly due to electron-hole compensation. Bulk T_d-WTe_2 [14], T_d-$MoTe_2$ [15, 16] as well as some of their alloys [17] are also known to be type-II Weyl fermions. These type-II Weyl fermions are characterized by touching points between electron- and hole-pocket, with strongly tilted Weyl cones [14] in the bulk, and Fermi-arc states on the surface. A number of angle-resolved photoemission spectroscopy (ARPES) studies of the electronic structure of T_d-WTe_2 [18–20], $MoTe_2$ [21–24] and $Mo_xW_{1-x}Te_2$ on the W rich side [25, 26] have found evidence for these features. Finally, in monolayer form, the T_d-TMDCs are two-dimensional topological insulators that display the quantum spin Hall effect [13, 27].

The rich electronic phenomenology associated with the semiconducting and metallic phases of these compounds has spurred intense interest in achieving precise control

---

[*] Current address: University of Michigan, Ann Arbor, Michigan 48109, USA
[†] apn2108@columbia.edu
[‡] osgood@columbia.edu

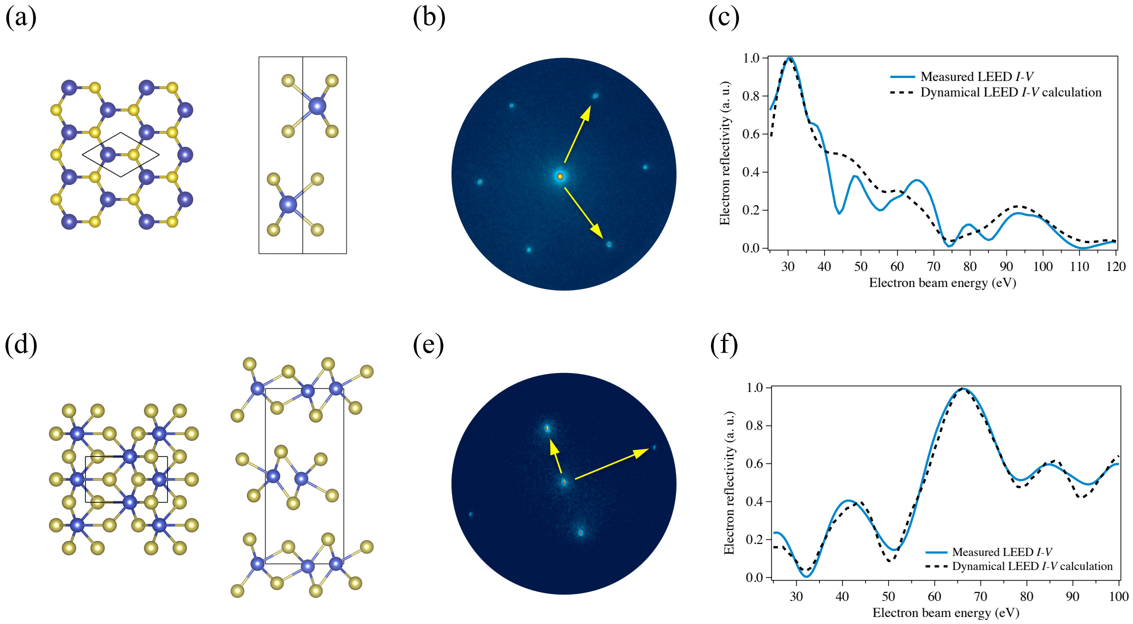

FIG. 1. **Crystalline structure of $2H$- and T_d- $Mo_{1-x}W_xTe_2$ crystals**. (a) Schematic of $2H$-phase atomic structure in top view (left) and sideview (right), (b) LEED pattern, and (c) μ-LEED I-V curve for $2H$-$Mo_{0.92}W_{0.08}Te_2$.(d) Schematic of T_d-phase atomic structure in topview (left) and sideview (right), (e) LEED pattern, and (f) μ-LEED I-V curve for T_d-$Mo_{0.84}W_{0.16}Te_2$. Blue spheres: Mo/W atoms; yellow spheres: Te atoms.

of transitions between these phases. Such phase engineering of TMDCs has recently been attempted using a variety of tuning parameters such as temperature, strain, chemical doping and electrostatic doping [13, 28–32]. Achieving reversible control of the phase transition is important for on-demand topological properties as well as for the development of technological applications such as phase-change memory devices [33, 34]. One of the chief difficulties in achieving this reversible control in the parent compounds $MoTe_2$ and WTe_2 is that the crystal are fairly stable at room temperature. In this context, alloying has been shown by some of us to play an important role in structural phase control [35]. Briefly, at room temperature, the thermodynamically stable phase of $MoTe_2$ is the semiconducting $2H$ polymorph. In contrast, the stable phase of WTe_2 is the semimetallic T_d polymorph. By using chemical alloying to produce the series $Mo_{1-x}W_xTe_2$, we showed the existence of a phase transition at around $x = 0.08$. We expect that as we approach the critical doping, the alloys become sensitive to dynamical tuning parameters such as strain and electrostatic doping, opening up new possibilities for structural control. As we approach this critical doping, we must understand the electronic structure of the alloys on either side of the phase transition in detail. In this work, we achieve understanding by performing synchrotron-based ARPES measurements of $Mo_{1-x}W_xTe_2$, as a function of W concentration, supported by structural characterization and density functional theory. The major findings of our study show that (i) the phase transition from $2H$ to T_d appears on the Mo-rich side (critical W concentration $x_c \sim 0.10 \pm 0.01$) of the alloy composition point, in contrast to the previously predicted value of 0.33 [36]; (ii) W doping results in an upward shift of the conduction band minimum, thus reducing the band inversion; and (iii) demonstration via density functional theory calculations that the interlayer coupling in this material is weaker than in the more widely studied TMDCs like MoS_2.

II. RESULTS AND DISCUSSION

The synthesis method for our crystals has been detailed in Ref.[35]. Prior to our ARPES measurements, the composition of the alloys was first determined with x-ray photoemission spectroscopy (XPS) [37]. The crystalline structure of $Mo_{1-x}W_xTe_2$ alloys was then investigated using selected-area low energy electron diffraction (μ-LEED) at room temperature. The well-defined hexagonal μ-LEED pattern (see Fig. 1(b)) acquired from $x = 0.08$ alloy, demonstrates that the alloys with $x < x_c$ crystallize in the $2H$-phase. In comparison, the rectangular μ-LEED pattern (Figs. 1 (e)) for a crystal of composition of $x = 0.16$ shows that moderate W substitution ($x > x_c$) stabilizes the T_d-phase at room temperature. Note that multiple locations were surveyed across the sample surface, and no phase coexistence was observed. In addition, to examine any

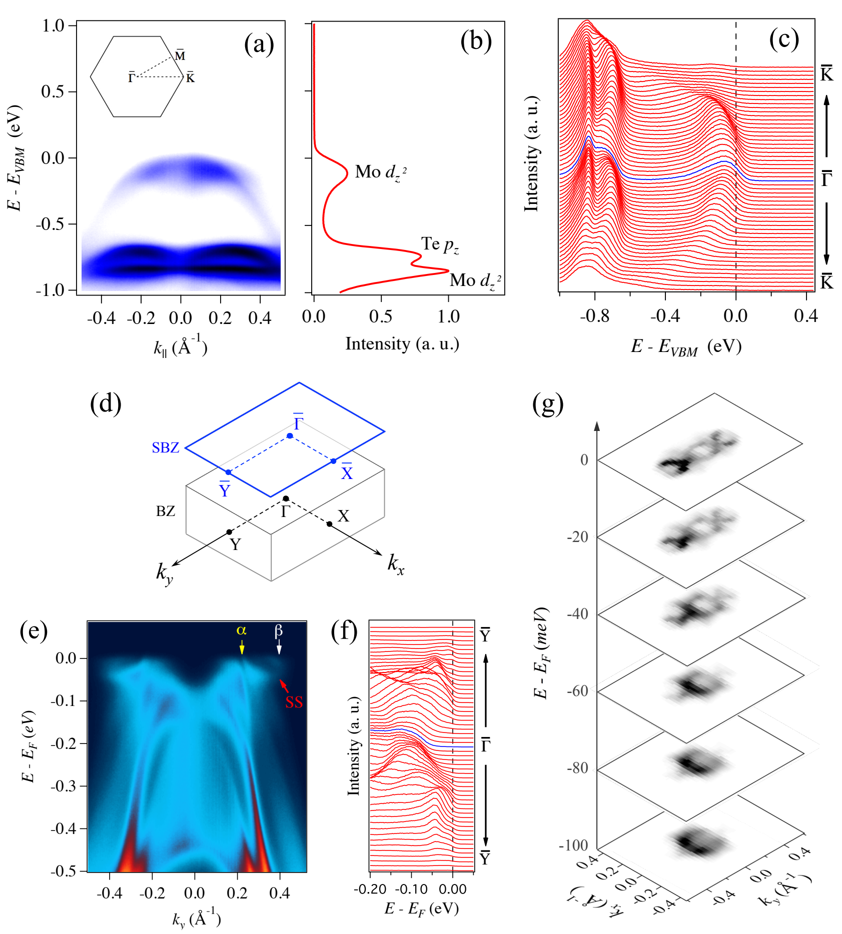

FIG. 2. **Electron structure of $Mo_{1-x}W_xTe_2$ alloys across critical W concentrations.** Electronic structure of 2H-$Mo_{0.94}W_{0.06}Te_2$ alloy (a) ARPES bandmap along $\bar{K}$-$\bar{\Gamma}$-$\bar{K}$ high symmetry direction, inset shows the surface Brillouin zone (b) Integrated spectrum and (c) EDCs plot of ARPES bandmap shown in (a). Electronic structure of T_d-$Mo_{0.80}W_{0.20}Te_2$ alloy (d) the bulk Brillouin zone (BZ) and projected (001) surface Brillouin zone (SBZ), (e) ARPES bandmap ($h\nu$ = 24 eV) along $\bar{Y}$-$\bar{\Gamma}$-$\bar{Y}$ high symmetry direction, (e) EDCs plot of band features near Fermi level (E_F), and (g) stack of constant energy maps.

major changes in crystal structure within surface layers, the surface structure of these $Mo_{1-x}W_xTe_2$ alloys was determined using dynamical LEED calculations[38–40]. The optimized surface structure for 2H- and T_d phase were obtained by fitting the calculated I-V curves to the measured ones. Fig. 1 (c) and (f) show the measured LEED-I-V (blue solid curve) for the (00) diffraction beam and calculated I-V (black dashed curve). Despite the discrepancy between the calculated and measured I-V curves in Fig. 1 (c), which is largely due to the effect of atomic vibration and surface roughness, a satisfactory Pendry R-factor of 5.2% and 0.5% is obtained for the 2H and T_d case, respectively, confirming a reliable determination of the surface structure. Our structural optimization indicated that the surface structure distinct from that in the bulk by $< 5\%$ relaxation, which is not significantly different enough to change the electronic structure.

ARPES measurements were then carried out to investigate the electronic structure of $Mo_{1-x}W_xTe_2$ alloys; to sharpen the spectra the measurements were made at low temperature. Figure. 2 (a) shows the ARPES bandmap of 2H-$Mo_{0.94}W_{0.06}Te_2$ alloy along the $\bar{K}$-$\bar{\Gamma}$-$\bar{K}$ high-symmetry direction of the surface Brillouin zone (see inset). The corresponding integrated spectrum (Fig. 2 (b)) shows that the main band features are derived from the Mo d_{z^2} and Te p_z orbitals. The conduction bands were not observed up to 1 eV above valence band maximum (VBM), confirming that the 2H-phase is semiconducting with a gap size $>$ 1 eV. The band features are further displayed as corresponding energy distribution curves (EDCs) plots in Fig. 2 (c). A parabolic fit of the topmost valence band yields a hole effective mass at $\bar{\Gamma}$ of $3.77m_0$ (where m_0 is the electron mass), which is larger than that of monolayer MoS_2 ($\sim 2.4m_0$). As revealed, the thickness-dependent electronic structure of MoS_2 [2], the topmost valence band at $\bar{\Gamma}$ decreases in energy with decreasing interlayer coupling strength, which leads to increasing hole effective

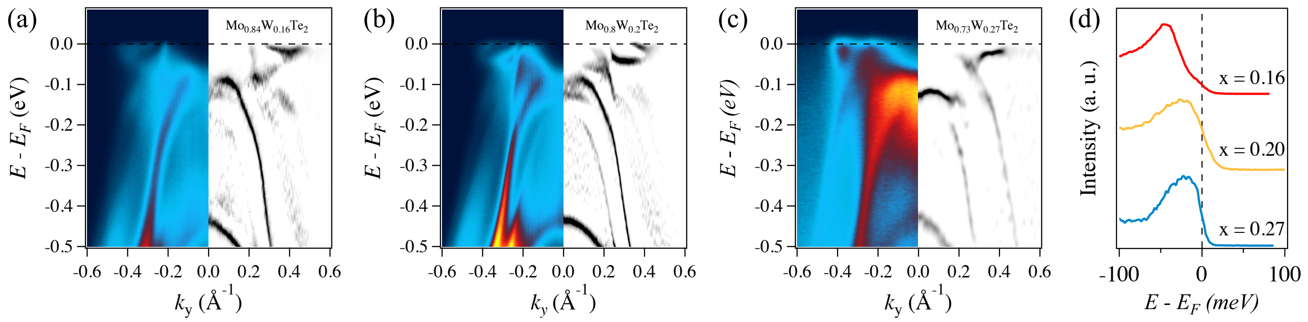

FIG. 3. **Electronic structure evolution for different T_d-$Mo_{1-x}W_xTe_2$ alloys with W concentrations.** ARPES bandmap (left) and corresponding second-derivative intensity plot (right) of T_d-$Mo_{1-x}W_xTe_2$ alloys along $\bar{Y}$-$\bar{\Gamma}$-$\bar{Y}$ high symmetry direction with (a) $x = 0.16$, (b) $x = 0.20$, and (c) $x = 0.27$. (d) Corresponding EDCs across conduction band minimum.

mass. The remarkably flat topmost valence band implies rather weak interlayer coupling in $2H$-$Mo_{0.94}W_{0.06}Te_2$ alloy.

In contrast to the semiconducting $2H$ phase, the ARPES bandmap (Fig. 2 (e)) of the T_d-phase (x = 0.2) along $\bar{Y}$-$\bar{\Gamma}$-$\bar{Y}$ (Fig. 2 (d)) high symmetry direction shows a metallic nature, in which a hole band (yellow arrow, α) and electron pocket (white arrow, β) both cross the Fermi level. In addition, the surface state (red, SS) protrudes into the electron pocket and almost overlaps with the hole band, which indicates that it is derived from a type-B surface [19]. These band features are further displayed in the EDC plot (Fig. 2 (f)). Figure 2 (g) shows the stack of constant-energy maps. In particular, a palmier-shaped hole pocket and an almond-shaped electron pocket are observed in the Fermi surface ($E = E_F$) map. The shape of the hole and electron pocket are qualitatively in good agreement with those of WTe_2, $MoTe_2$, and $Mo_{1-x}W_xTe_2$ alloys. The sizes of the hole and electron pockets increase and decrease with increasing binding energy, respectively. We have comprehensively measured the electronic structure evolution of the T_d phase as a function of W concentrations. A side-by-side comparison of the electronic structure is made between $x = 0.16$, $x = 0.20$, and $x = 0.27$. As shown in the ARPES bandmaps and corresponding second derivative plots in Fig. 3(a)-(c), the overlap in energy between valence and conduction band decreases with increasing W concentration. Such overlap can be characterized by the energy position of the conduction band minimum (CBM), as shown in the EDC plots (Fig. 3(d)). The CBM of $x = 0.16$ is located at $\sim 50\,\text{meV}$, which is comparable with that of pure T_d-$MoTe_2$ (60 meV) [21]. As the W concentration increases, the CBM shifts towards the Fermi level, and in the $x = 0.27$ alloy, the overlap is significantly suppressed, given the large content of Mo relative to W. While we do not directly visualize the Weyl crossings in this data set, it is clear that the change in the band inversion also tunes the separation between Weyl points and consequently the surface state band structure.

To further investigate the band inversion observed here, we use density functional theory calculations to study the evolution of the electronic structure with alloying. Our previous photon energy-dependent ARPES studies [35] and theoretical calculations [41] have revealed that the dispersion along k_z direction shows two-dimensional character. Here, we employ a model at the 2D limit by considering only one unit cell (1UC) thickness of the T_d structure (see Fig. 1(d)). Figure 4(a) shows the calculated hole band and electron pocket as a function of W concentration. As the W concentration increases, the hole band slightly sinks while the electron pocket rapidly shifts upwards. Our 1UC model captures the measured band inversion evolution very well. This result further confirms the 2D character of the electronic structure. First principle calculations can also give insight into the structural stability of the $2H$ and T_d phases as a function of alloying. To clarify this question, we first investigated both the $2H$ and T_d phase of the bulk and monolayer structures of pure $MoTe_2$ and WTe_2. To directly compare the total energy between $2H$ and T_d phase with different W concentrations, we employ an expanded supercell containing 12(24) Mo/W atoms for 1UC (bulk) cases. This supercell can be regarded as a 3×2 supercell of the primitive cell for T_d phase. The energy difference per Mo/W atom between $2H$ and T_d are shown in Fig. 4(b). The energy difference as a function of doping value x is nearly a linear relationship, which leads to a phase transition point at $x = 0.25$ for bulk and $x = 0.13$ for 1UC case. Here, the phase transition point predicted by the bulk model is close to that of the previous study, while the 1UC model more accurately captures the measured critical doping value ($x_c \sim 0.10$), which further confirms that $Mo_{1-x}W_xTe_2$ crystal is close to a 2D system rather than a vdW system.

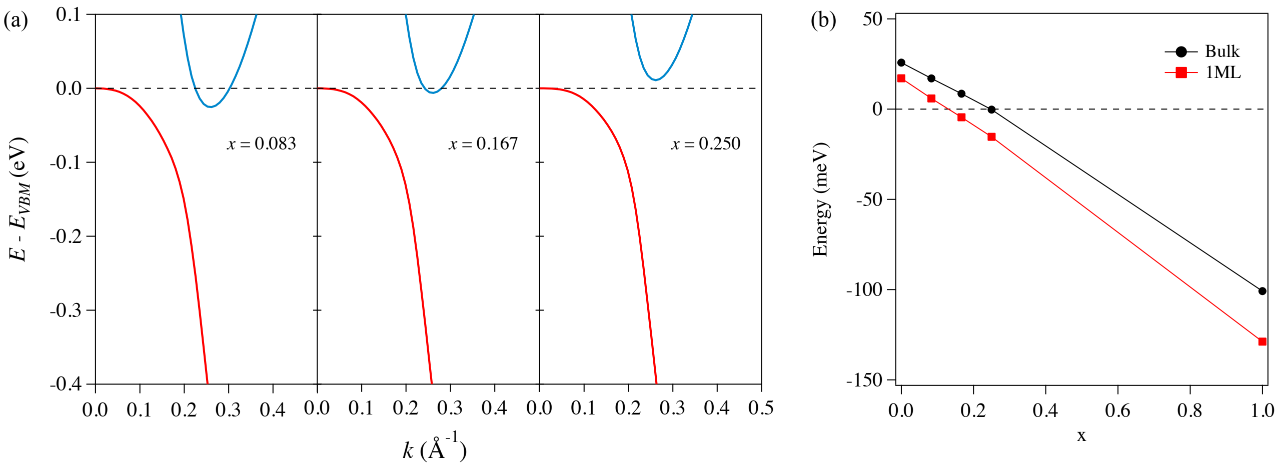

FIG. 4. (a) DFT calculated hole band and electron pocket with various W concentrations. The valence band maximum (VBM) is denoted as dashed line. (b) The calculated energy difference between 2H and T_d phase as a function of doping value x of $Mo_{1-x}W_xTe_2$ for both bulk and 1UC.

III. CONCLUSION

In conclusion, we investigated the structural phase transition and electronic structure evolution of $Mo_{1-x}W_xTe_2$ alloys using ARPES and DFT calculations. Our results show that a critical W concentration of $x \sim 0.10$ triggers a phase transition from 2H to T_d phase, and in the T_d phase, topological strength is significantly suppressed by increasing W doping. The phase transition point and electronic structure evolution is captured well by the DFT calculations using a 1UC model, indicating the 2D character of this material due to weak interlayer coupling.

IV. METHODS

Angle-resolved photoemission spectroscopy. ARPES measurements were performed in part at the Dreamline beamline of the Shanghai Synchrotron Radiation Facility (SSRF) with a Scienta D80 analyzer, and in part at the beamlines 5-2 and 5-4 of the Stanford Synchrotron Radiation Lightsource (SSRL) with Scienta R4000 and D80 analyzers, respectively. The energy and angular resolutions were set to better than 10 meV and 0.1°, respectively. The samples were measured between 30 K and 60 K with a base pressure $< 5 \times 10^{-11}$ Torr. The ARPES data were collected within 12 hours after cleavage, during which time no signature of surface degradation was observed.

Low energy electron microscopy. μ-LEED measurements were performed at the Center for Functional Nanomaterials, Brookhaven National Laboratory using an ELMITEC AC-LEEM system. In this system, the sample was cleaved *in situ* at room temperature. The spatial resolution is <3 nm in the LEEM mode. The electron-beam spot size in the μ-LEED mode is 5 µm in diameter. LEED intensity-voltage (I-V) curves are acquired by measuring the LEED intensity as a function of incident electron energies.

First-principles electronic structure calculation. Density functional theory calculation was carried out using a VASP package [42] with a projector augmented plane-wave potential [43]. The exchange-correlation energy was described by the generalized gradient approximation in Perdew, Burke, and Ernzerhof (PBE) form [44]. The Brillouin zone of the orthogonal unit cell of T_d-$Mo_{1-x}W_xTe_2$ were sampled by a 7×12×3 k-point mesh. The energy cutoff was set to 440eV. Van der Waals interactions were incorporated within the Tkatchenko-Scheffler method [45]. Spin-orbit coupling was also included for structural optimization. All structures were optimized until the atomic force on each atom with both Hellmann-Feynman and van der Waals terms were taken into acount, is less than 1meV/Å. For one unit cell case, a vacuum layer of 15 Å is used to build 2D slabs.

Dynamical LEED Calculation. The codes from Adams *et al.* [46], which were developed from the programs of Pendry [47] and Van Hove and Tong [48], were used in the dynamical LEED calculations. The lattice constants of WTe_2 are a = 6.282 Å, b = 3.496 Å, c = 14.07 Å [49]. The lattice constants of $MoTe_2$ are a = 6.335 Å, b = 3.477 Å, c = 13.883 Å [15]. As the lattice contant difference between $MoTe_2$ and WTe_2 is less than 1.5%, we use the weighed average as the lattice contants of $Mo_{1-x}W_xTe_2$ alloys. The Debye temperature for $Mo_{1-x}W_xTe_2$ was set as 210 K. The inner potential of $Mo_{1-x}W_xTe_2$ is set as 10.1 eV. 12 (L = 11) phase shifts are used in the calculation.

V. ACKNOWLEDGEMENTS

The LEEM/LEED research was carried out in part at the Center for Functional Nanomaterials, Brookhaven National Laboratory, was supported by the U.S. Department of Energy, Office of Basic Energy Sciences, under Contract No. DE-SC0012704. The work of R.M.O., J.D., W.J. and Y.L. was financially supported by the U.S. Department of Energy under Contract No. DE-FG 02-04-ER-46157. T.S., J.H., and A.N.P. were supported by NSF MRSEC program through Columbia (DMR-1420634). In addition, Z.W.D., and K.P. were supported by NSF DMR 1006863. J.X.Y. and J.Z. were supported by the U.S. Department of Energy (DOE), Office of Science, Basic Energy Sciences (BES) under Award No. DE-SC0016424 and used the Extreme Science and Engineering Discovery Environment (XSEDE) under Grant No. TG-PHY170023. R.L. and S.C.W. were supported by the National Natural Science Foundation of China (No. 11274381). J.Z.M., T.Q., and H.D. were supported by the Ministry of Science and Technology of China (No. 2015CB921300, No. 2013CB921700), the National Natural Science Foundation of China (No. 11474340, No. 11234014), and the Chinese Academy of Sciences (No. XDB07000000). Use of the SSRL was supported by the U.S. Department of Energy, Office of Basic Energy Sciences, under Contract No. DE-AC02-76SF00515. E.J.G.S. acknowledges the use of computational resources from the UK national high-performance computing service (ARCHER) for which access was obtained via the UKCP consortium (EPSRC grant ref EP/K013564/1); the UK Materials and Molecular Modelling Hub for access to THOMAS supercluster, which is partially funded by EPSRC (EP/P020194/1). The Queens Fellow Award through the grant number M8407MPH, the Enabling Fund (A5047TSL), and the Department for the Economy (USI 097) are also acknowledged.

---

[1] K. F. Mak, C. Lee, J. Hone, J. Shan, and T. F. Heinz, Physical Review Letters **105**, 136805 (2010).

[2] W. Jin, P.-C. Yeh, N. Zaki, D. Zhang, J. T. Sadowski, A. Al-Mahboob, A. M. van Der Zande, D. A. Chenet, J. I. Dadap, I. P. Herman, *et al.*, Physical Review Letters **111**, 106801 (2013).

[3] Y. Zhang, T.-R. Chang, B. Zhou, Y.-T. Cui, H. Yan, Z. Liu, F. Schmitt, J. Lee, R. Moore, Y. Chen, *et al.*, Nature Nanotechnology **9**, 111 (2014).

[4] D. Xiao, G.-B. Liu, W. Feng, X. Xu, and W. Yao, Physical Review Letters **108**, 196802 (2012).

[5] K. F. Mak, K. He, J. Shan, and T. F. Heinz, Nature Nanotechnology **7**, 494 (2012).

[6] T. Cao, G. Wang, W. Han, H. Ye, C. Zhu, J. Shi, Q. Niu, P. Tan, E. Wang, B. Liu, *et al.*, Nature Communications **3**, 887 (2012).

[7] Q. H. Wang, K. Kalantar-Zadeh, A. Kis, J. N. Coleman, and M. S. Strano, Nature Nanotechnology **7**, 699 (2012).

[8] K. F. Mak, K. L. McGill, J. Park, and P. L. McEuen, Science **344**, 1489 (2014).

[9] H. Zeng, J. Dai, W. Yao, D. Xiao, and X. Cui, Nature Nanotechnology **7**, 490 (2012).

[10] K. Zhang, C. Bao, Q. Gu, X. Ren, H. Zhang, K. Deng, Y. Wu, Y. Li, J. Feng, and S. Zhou, Nature Communications **7** (2016).

[11] M. N. Ali, J. Xiong, S. Flynn, J. Tao, Q. D. Gibson, L. M. Schoop, T. Liang, N. Haldolaarachchige, M. Hirschberger, N. Ong, *et al.*, Nature **514**, 205 (2014).

[12] L. Thoutam, Y. Wang, Z. Xiao, S. Das, A. Luican-Mayer, R. Divan, G. Crabtree, and W. Kwok, Physical Review Letters **115**, 046602 (2015).

[13] D. H. Keum, S. Cho, J. H. Kim, D.-H. Choe, H.-J. Sung, M. Kan, H. Kang, J.-Y. Hwang, S. W. Kim, H. Yang, *et al.*, Nature Physics **11**, 482 (2015).

[14] A. A. Soluyanov, D. Gresch, Z. Wang, Q. Wu, M. Troyer, X. Dai, and B. A. Bernevig, Nature **527**, 495 (2015).

[15] Y. Sun, S.-C. Wu, M. N. Ali, C. Felser, and B. Yan, Physical Review B **92**, 161107 (2015).

[16] Z. Wang, D. Gresch, A. A. Soluyanov, W. Xie, S. Kushwaha, X. Dai, M. Troyer, R. J. Cava, and B. A. Bernevig, Physical Review Letters **117**, 056805 (2016).

[17] T.-R. Chang, S.-Y. Xu, G. Chang, C.-C. Lee, S.-M. Huang, B. Wang, G. Bian, H. Zheng, D. S. Sanchez, I. Belopolski, *et al.*, Nature communications **7**, 10639 (2016).

[18] J. Sánchez-Barriga, M. Vergniory, D. Evtushinsky, I. Aguilera, A. Varykhalov, S. Blügel, and O. Rader, Physical Review B **94**, 161401 (2016).

[19] F. Y. Bruno, A. Tamai, Q. Wu, I. Cucchi, C. Barreteau, A. De La Torre, S. M. Walker, S. Riccò, Z. Wang, T. Kim, *et al.*, Physical Review B **94**, 121112 (2016).

[20] C. Wang, Y. Zhang, J. Huang, S. Nie, G. Liu, A. Liang, Y. Zhang, B. Shen, J. Liu, C. Hu, *et al.*, Physical Review B **94**, 241119 (2016).

[21] K. Deng, G. Wan, P. Deng, K. Zhang, S. Ding, E. Wang, M. Yan, H. Huang, H. Zhang, Z. Xu, J. Denlinger, A. Fedorov, H. Yang, W. Duan, H. Yao, Y. Wu, S. Fan, H. Zhang, X. Chen, and S. Zhou, Nature Physics **12**, 1105 (2016).

[22] L. Huang, T. M. McCormick, M. Ochi, Z. Zhao, M.-T. Suzuki, R. Arita, Y. Wu, D. Mou, H. Cao, J. Yan, N. Trivedi, and A. Kaminski, Nature Materials **15**, 1155 (2016).

[23] A. Tamai, Q. S. Wu, I. Cucchi, F. Y. Bruno, S. Ricc, T. K. Kim, M. Hoesch, C. Barreteau, E. Giannini, C. Besnard, A. A. Soluyanov, and F. Baumberger, Physical Review X **6**, 031021 (2016).

[24] J. Jiang, Z. Liu, Y. Sun, H. Yang, C. Rajamathi, Y. Qi, L. Yang, C. Chen, H. Peng, C. Hwang, *et al.*, Nature Communications **8**, 13973 (2017).

[25] I. Belopolski, D. S. Sanchez, Y. Ishida, X. Pan, P. Yu, S.-Y. Xu, G. Chang, T.-R. Chang, H. Zheng, N. Alidoust, *et al.*, Nature Communications **7**, 13643 (2016).

[26] I. Belopolski, S.-Y. Xu, Y. Ishida, X. Pan, P. Yu, D. S. Sanchez, H. Zheng, M. Neupane, N. Alidoust, G. Chang, *et al.*, Physical Review B **94**, 085127 (2016).

[27] X. Qian, J. Liu, L. Fu, and J. Li, Science **346**, 1344 (2014).

[28] K.-A. N. Duerloo, Y. Li, and E. J. Reed, Nature Communications **5**, 4214 (2014).

[29] S. Cho, S. Kim, J. H. Kim, J. Zhao, J. Seok, D. H. Keum, J. Baik, D.-H. Choe, K. Chang, K. Suenaga, *et al.*, Science **349**, 625 (2015).

[30] K.-A. N. Duerloo and E. J. Reed, ACS Nano **10**, 289 (2015).

[31] Y. Li, K.-A. N. Duerloo, K. Wauson, and E. J. Reed, Nature Communications **7**, 10671 (2016).

[32] Y. Wang, J. Xiao, H. Zhu, Y. Li, Y. Alsaid, K. Y. Fong, Y. Zhou, S. Wang, W. Shi, Y. Wang, *et al.*, Nature **550**, 487 (2017).

[33] M. Wuttig and N. Yamada, Nature Materials **6**, 824 (2007).

[34] Q. Wang, E. T. Rogers, B. Gholipour, C.-M. Wang, G. Yuan, J. Teng, and N. I. Zheludev, Nature Photonics **10**, 60 (2016).

[35] D. Rhodes, D. Chenet, B. Janicek, C. Nyby, Y. Lin, W. Jin, D. Edelberg, E. Mannebach, N. Finney, A. Antony, *et al.*, Nano Letters **17**, 1616 (2017).

[36] C. Zhang, S. KC, Y. Nie, C. Liang, W. G. Vandenberghe, R. C. Longo, Y. Zheng, F. Kong, S. Hong, R. M. Wallace, *et al.*, ACS nano **10**, 7370 (2016).

[37] See Supplemental Material for determination of stoichiometry of alloys using XPS.

[38] Z. Dai, W. Jin, M. Grady, J. T. Sadowski, J. I. Dadap, R. M. Osgood, and K. Pohl, Surface Science **660**, 16 (2017).

[39] W. Jin, S. Vishwanath, J. Liu, L. Kong, R. Lou, Z. Dai, J. T. Sadowski, X. Liu, H.-H. Lien, A. Chaney, *et al.*, Physical Review X **7**, 041020 (2017).

[40] Z. Dai, W. Jin, J.-X. Yu, M. Grady, J. T. Sadowski, Y. D. Kim, J. Hone, J. I. Dadap, J. Zang, R. M. Osgood Jr, *et al.*, Physical Review Materials **1**, 074003 (2017).

[41] D. Rhodes, R. Schönemann, N. Aryal, Q. Zhou, Q. Zhang, E. Kampert, Y.-C. Chiu, Y. Lai, Y. Shimura, G. McCandless, *et al.*, Physical Review B **96**, 165134 (2017).

[42] G. Kresse and J. Furthmüller, Physical review B **54**, 11169 (1996).

[43] P. E. Blöchl, Physical review B **50**, 17953 (1994).

[44] J. P. Perdew, K. Burke, and M. Ernzerhof, Physical review letters **77**, 3865 (1996).

[45] A. Tkatchenko and M. Scheffler, Physical review letters **102**, 073005 (2009).

[46] D. L. Adams, Surface Science **519**, 157 (2002).

[47] J. Pendry and G. P. Alldredge, Physics Today **30**, 57 (1977).

[48] M. A. Van Hove and S. Y. Tong, *Surface crystallography by LEED: theory, computation and structural results*, Vol. 2 (Springer Science & Business Media, 2012).

[49] B. E. Brown, Acta Crystallographica **20**, 268 (1966).